NIH Public Access
Author Manuscript
Tsinghua Sci Technol. Author manuscript; available in PMC 2010 June 28.

Published in final edited form as:
Tsinghua Sci Technol. 2010 February ; 15(1): 79–86. doi:10.1016/S1007-0214(10)70013-4.

Dual-Energy Technique at Low Tube Voltages for Small Animal Imaging*

Seungryong CHO, **Emil Y SIDKY**, **Junguo BIAN**, and **Xiaochuan PAN****
Department of Radiology, University of Chicago, Chicago, IL 60637, USA

Abstract

We investigate the feasibility of dual-energy method for image contrast enhancement in small animal studies using a low kV X-ray radiographic system. A robust method for X-ray spectrum estimation from transmission measurements, based on expectation-maximization (EM) method, is applied to an X-ray specimen radiographic system for dual energy imaging of a mouse. From transmission measurements of two known attenuators at two different X-ray tube voltages, the X-ray energy spectra are reconstructed using the EM-based method. From the spectra information thus obtained, the transmission data for bone and soft tissue in terms of various thicknesses are generated. Two polynomial functions of transmission data are then sought for to fit the inverted thicknesses of bone and soft-tissue. Scatters in cone-beam projection data acquired at two X-ray energies were corrected. From the scatter-corrected data, a bone thickness map is separated from a soft-tissue thickness map by use of the polynomial functions.

Keywords

dual-energy; specimen radiography; spectrum estimation

Introduction

Recently, desktop microCT systems or specimen X-ray radiographic systems have been widely used for small animal studies or diagnostic research. Some of these systems have X-ray source tubes that can operate only up to about 40 kV, which is designed so for the optimum image contrast[1] in applications to specimen imaging or small animal imaging. The dual-energy imaging approach can be used for improving the image contrast further in these applications.

Dual-energy imaging exploits the differential relative attenuation of X-ray photons exhibited by soft-tissue and bony structures at different X-ray energies to generate a pair of images that separate those structures, thereby reducing the confounding visual effects of structure noise. It was also investigated to separate fat image from other tissue image in obesity studies[2]. Different X-ray energies can be achieved by using either different source voltages or different X-ray energy windows to collect the data[3]. Most previous dual-energy studies are based on wide separation of the X-ray energies with the upper energy of about 100 keV. However, dual-energy imaging can be challenging for the desktop systems having low maximum kV such as 40 kV. We demonstrate the feasibility of dual-energy imaging for such low kV X-ray systems in this work.

*Supported by the National Institutes of Health (Nos. EB00225 and CA120540). S. Cho was supported in part by the DoD Predoctoral Training Grant (No. PC 061210).

**To whom correspondence should be addressed. xpan@uchicago.edu; Tel: 1-773-702-1293 .

NIH-PA Author Manuscript
NIH-PA Author Manuscript
NIH-PA Author Manuscript

NIH-PA Author Manuscript

NIH-PA Author Manuscript

NIH-PA Author Manuscript

Dual-energy methods involve a calibration procedure that establishes the relationship between measurements and material thicknesses of two materials. Conventional calibration methods are based on basis material decomposition where the reference samples are used for the basis materials, even though the material system under investigation may have different material compositions. Existing spectral calibration methods[4] can incorporate the spectral information, determined by emitted X-ray spectrum and the spectral absorption of the detector system, to calibrate the material system under investigation. Therefore the calibration can be done independently of the nature of the materials under investigation. Knowledge of the X-ray spectrum in diagnostic imaging is important for, in addition to dual-energy imaging, a variety of applications such as determining patient dose, correction for beam-hardening artifacts, and quantitative computed tomography (CT)[5-7]. X-ray spectrum can be estimated from transmission measurements using a phantom of known dimensions and composition[8-13]. However, the problem of estimating the spectrum from the transmission data can be mathematically unstable because the linear system of measurement model is highly ill-conditioned. Based on the observation that the measured data function can be interpreted as a positive integral equation, we have previously proposed a robust and flexible EM-based method to obtain the X-ray spectrum from transmission data[14]. The proposed EM method was compared in computer simulation studies to other approaches including direct analysis with singular-value decomposition (SVD), and the numerical results showed that the proposed EM method yields results superior to those from other approaches[14].

The EM-based method is applied to estimate the spectral properties of a specimen radiographic system, which can operate between 20 kV and 35 kV, and utilize the spectral information for dual-energy imaging of a mouse. Spectra at two different source voltages are estimated from transmission measurements of aluminum and lucite in a narrow beam geometry, and the obtained spectral information is used to generate transmission data for bone and soft-tissue of a mouse. A correction method employing a convolution kernel is used for scatter correction in the projection data acquired by the system. After scatter correction, we convert two projection images of a mouse achieved at different X-ray energies into the bone thickness map and the soft-tissue thickness map using polynomial inversion functions.

1 Spectrum Estimation

In this section, we describe the EM-based method for X-ray energy spectrum estimation of the specimen radiographic system described below from transmission measurements.

1.1 Specimen radiographic system

The system consists of a microfocal X-ray source, and a CsI-coupled CMOS detector. The microfocal X-ray source (MX-20, Faxitron, USA), comprised of a tungsten anode with beryllium exit window, can be operated between 20 to 35 kV, and can yield a focal spot size of 20 μm. The 14-bit digital camera (Bioptics, USA) consists of a CsI scintillator and an array of 2048×1024 of CMOS thin-film transistors and photodiodes with a pixel size of about 50 μm. Since the Faxitron system is designed for specimen radiographic purposes, the available tube voltage range is relatively narrow and low. The tube current of the Faxitron system is fixed by 300 μA.

1.2 EM-based method

The transmission data can be modeled as a linear function of the X-ray source spectrum, which is given by

$$t(L) = \int_E s(E)\ \exp\left[-\int_L \mu(E,x)\,\mathrm{d}l\right]\mathrm{d}E \tag{1}$$

NIH-PA Author Manuscript

NIH-PA Author Manuscript

NIH-PA Author Manuscript

where $t(L)$ represents the transmission through a phantom with attenuation map $\mu(E, x)$ and pathlength L. E is the X-ray energy, l denotes position along the transmission path, and $s(E)$ represents the X-ray source spectrum. Note the model in Eq. (1) is idealized, e.g., noise and scatter are not incorporated, and the spectrum $s(E)$ actually represents the product of the X-ray source spectrum and the detector spectral response. The task of estimating the spectrum in this work is to determine $s(E)$ from knowing $t(L)$ and $\mu(E, x)$.

In practical applications, only discrete data are available. Therefore, the transmission model in Eq. (1) can be discretized and be converted to a linear system,

$$\boldsymbol{d}_m = \sum_n A_{mn} \boldsymbol{c}_n \tag{2}$$

where the data vector $\boldsymbol{d}_m$ is the finite set of transmission measurements; the vector $\boldsymbol{c}_n$ represents the expansion coefficients of the X-ray spectrum in terms of a selected basis set $\emptyset_n(E)$,

$$s(E) = \sum_{n=1}^{N} \boldsymbol{c}_n \phi_n(E) \tag{3}$$

and the system matrix $\boldsymbol{A}$, with its elements defined as

$$A_{mn} = \int_E \phi_n(E) \exp\left[-\int_{L_m} \mu(E, x)\, \mathrm{d}l\right] \mathrm{d}E \tag{4}$$

depends on the spectrum representation, scanning configuration, and the phantom. The task of estimating $s(E)$ is now equivalent to that of estimating the expansion coefficients $\boldsymbol{c}_n$ from knowing A_{mn} and $\boldsymbol{d}_m$. Linear B-splines were used as basis functions in this work.

The EM-based method can be used to seek for a solution to Eq. (2) when the spectrum basis functions are positive and when the data model is a positive integral equation. It seeks to recover the spectral coefficients, $\boldsymbol{c}_n$, from the transmission data, $\boldsymbol{d}_m$, and has a multiplicative update equation,

$$c_n^{(k+1)} = c_n^k \frac{\sum_m \boldsymbol{A}_{nm}^{\mathrm{T}} \frac{\boldsymbol{d}_m}{\sum_{n'} A_{mn'} c_{n'}^k}}{\sum_m \boldsymbol{A}_{nm}^{\mathrm{T}}} \tag{5}$$

where the index k indicates the iteration numbers. As shown previously[14], if a realistic spectrum is employed as an initial guess, the results from the EM-based method can be very accurate. Whereas, if no prior information is used, e.g., all coefficients set to unity, the resulting spectrum will have broad features that match the true spectrum, but details may not be completely recoverable. For the task of spectrum estimation to reproduce the transmission data for a variety of materials, the EM results without prior information of the spectrum may be sufficient.

1.3 Estimated spectrum

Transmission measurements for spectrum estimation were performed with a number of slabs made of aluminum and of lucite. The slabs have a uniform thickness for each material. A narrow

NIH-PA Author Manuscript

NIH-PA Author Manuscript

NIH-PA Author Manuscript

beam geometry as shown in Fig. 1 was used in the transmission measurements to effectively remove scatter[15,16]. A lead block, which can be called a collimator, having an aperture of 0.2 mm diameter was placed in front of the phantom materials. The projection image of this aperture on the detector was as small as 16 pixels (4 by 4), which is believed to be much smaller than the typical size of a scatter kernel on a detector plane. Peak value of the averaged image of the aperture projections on the 16 pixels was selected to represent the measured transmission. The tube voltage and the mAs were kept constant for each exposure.

For a given exposure, the transmission was measured as a function of the phantom thickness. Tube voltages of 22 kV and 35 kV were selected for generating two different energy spectra. Additional aluminum filtration was used to enhance the high-shift in the energy spectrum for the case of 35 kV. For convenience, we represent the case of the tube voltage of 35 kV with aluminum filtration as simply 35 kV throughout this paper. The measured transmission characteristics are plotted with solid squares in Fig. 2 and Fig. 3 for aluminum and for lucite, respectively.

The estimated spectra by use of the EM method are shown in Fig. 4. No prior information was applied for the initial estimate in the EM algorithm and the calculated spectra appear to be reasonably separated. From the estimated spectra, we calculated transmission characteristics for aluminum and lucite using the attenuation coefficients as a function of energy. The calculated transmission curves are represented as solid triangles in Fig. 2 and Fig. 3. The calculated transmission curves are in good agreement with the measured transmission curves. Using the estimated spectra and the attenuation coefficients of bone and tissue as a function of energy, we generated transmission data for bone and soft-tissue.

Figure 5 shows the calculated transmission data for (a) bone and (b) soft-tissue. Solid square represents the data calculated for the tube voltage of 22 kV and solid triangle for 35 kV. The transmission data are going to be used in dual-energy imaging of a mouse as described in the following section.

2 Dual-Energy Method

In this section, we use the estimated X-ray spectra for obtaining dual-energy images of a mouse.

2.1 Dual-energy decomposition

For a single measurement ray, we performed two measurements T_{low} and T_{high} with low and high energy spectra. The measurements can be modeled as

$$\begin{aligned} T_{\text{low}}(L_1, L_2) &= -\ln \int_E s_{\text{low}}(E)\ \exp\left[-L_1\mu_1(E) - L_2\mu_2(E)\right] \mathrm{d}E, \\ T_{\text{high}}(L_1, L_2) &= -\ln \int_E s_{\text{high}}(E)\ \exp\left[-L_1\mu_1(E) - L_2\mu_2(E)\right] \mathrm{d}E \end{aligned} \tag{6}$$

where the right-hand side of the equations embodies a dual-energy approximation by writing the attenuation factor as the pathlengths of two materials multiplied by the attenuation of two materials. Note that T_{low} and T_{high} are not the measured intensity but logarithmic of the normalized intensity. The attenuation coefficients of two materials, which are bone and soft-tissue in this work, can be obtained from atomic data presented in NIST Report No. 5632 [17].

The task of dual-energy radiography is to recover L_1 and L_2 from the measurements T_{low} and T_{high}. It constitutes, therefore, an inversion problem for a system of nonlinear equations. Equation (6) can be numerically inverted to obtain the pathlengths of two materials from the measurements. Polynomial functions of up to fifth order of T_{high} and up to first order of

NIH-PA Author Manuscript

NIH-PA Author Manuscript

NIH-PA Author Manuscript

($T_{low} - T_{high}$), as shown in Eq. (7), were chosen to best fit numerically inverted L_1 and L_2 from Eq. (6). The fitting parameters are summarized in Table 1. L_1 and L_2 stand for the thicknesses of bone and soft-tissue, respectively.

$$L_1\left(T_{low}, T_{high}\right) = \sum_{i=0}^{5} T_{high}^{i} \left[\sum_{j=0}^{1} a_{ij}\left(T_{low} - T_{high}\right)^{j}\right],$$
$$L_2\left(T_{low}, T_{high}\right) = \sum_{i=0}^{5} T_{high}^{i} \left[\sum_{j=0}^{1} b_{ij}\left(T_{low} - T_{high}\right)^{j}\right] \quad (7)$$

2.2 Scatter correction

Scatter correction is necessary because the dual energy method described above and the spectrum estimation explained in Section 2 are based on the scatter-free data model. Even though it is known that the amount of scatter can be relatively low for small objects like mice [18], a proper rejection of scatter is still necessary for successful dual-energy imaging.

Methods have been proposed to correct for the scatter in cone-beam projections using hardware or software or both[19-24]. However, in a specimen radiographic system, the use of scatter grids, beam stoppers, and primary beam modulators may be very difficult due to the small size of the detector elements. A common technique for estimating scatter in such small systems, therefore, is to use software approaches.

A convolution filtering method is used to estimate the scatter fields using an isotropic Gaussian kernel. The scale factor, which is related to the scatter fraction (SF), and the FWHM of the Gaussian kernel were parametrized. A 1.5 cm thick lucite plate was used as a scatter phantom to simulate the mouse. To obtain the scatter fraction, the narrow beam geometry was used again with the lucite phantom. The pixel value of the projection of the aperture of the lead collimator used in the transmission measurements was used as the primary beam intensity, and the reference pixel value without the lead collimator was used as the primary-plus-scatter beam intensity. We obtained SF's of 8% and 10% for high and low energy spectrum respectively from the measurements. Edge spread curve (ESC) of the projection images of a square lead block with and without the lucite phantom was analyzed to optimize the FWHM of the Gaussian kernel. The ESC of the projection image of a lead block without the scatter phantom was assumed to reflect a primary beam profile. The measured primary beam profile was scaled such that the maximum plateau of the profile was placed at the level of (1–SF)×the maximum plateau of the primary-plus-scatter beam profile. A Gaussian kernel was then sought for to fit the ESC of the lead projection image with the lucite phantom by convolving the primary beam profile.

FWHM of 140 pixels was selected for the Gaussian kernel to best fit the measured primary-plus-scatter beam profiles at both high and low energy spectra. Figure 6 shows the measured ESC of the lead projection with and without the lucite phantom, and it also shows the fitted curves using the Gaussian kernel with FWHM of 140 pixels.

Since the projection images of the mouse contain both the primary and the scatter information, we cannot apply our Gaussian kernel for convolution to obtain scatter fields in theory. However, it is not unreasonable to use the primary-plus-scatter images to approximate primary images as long as the Gaussian kernel is normalized to SF/(1+SF), because the SF is relatively low.

2.3 Dual-energy images

We have applied our dual-energy method described above to obtain the bone thickness map and the softtissue thickness map of a mouse. For convenience, high energy spectrum stands for the X-ray spectrum at 35 kV with additional aluminum filtration, and low energy spectrum

NIH-PA Author Manuscript

NIH-PA Author Manuscript

NIH-PA Author Manuscript

for the X-ray spectrum at 22 kV hereafter. Figure 7 shows projection images of the mouse at high energy spectrum and low energy spectrum. After subtracting the scatter fields from the projection images, we calculated bone thickness map and tissue thickness map from Eq. (7). The results are shown in Fig. (8) for tissue and bone, respectively. The bone thickness map is successfully separated from the tissue thickness map although the images show nonnegligible noise.

3 Discussion

We have investigated and demonstrated the feasibility of dual-energy imaging for a specimen radiographic system with a low maximum kV X-ray source to improve the image contrast. Although dual-energy methods have been widely used in small animal studies, there has been no attempt, to our best knowledge, to investigate them for a system with a low maximum kV such as 40 kV. A spectral calibration approach has been used to calibrate the material system under investigation. We have applied the EM-based method to obtain spectral information of the system from the transmission measurements with known attenuators. Transmission measurements, performed in a narrow beam geometry, agree well with the calculated transmission data from the estimated X-ray spectrum. The estimated spectrum from the measured transmission data is acceptable although the details of the actual spectrum might be different from the estimated one. Since no prior knowledge on the spectrum was fed into the EM-based method, only the asymptotic behavior is supposed to match well with the true spectrum. It is also worth while to note that the estimated spectrum actually represents the product of the X-ray source spectrum and the detector spectral response, which is the spectral quantity of interest for dual-energy methods.

A convolution method based on a Gaussian kernel was used to correct for the scatter in projection images of a mouse. Scatter fraction was determined from the transmission measurements, and the FWHM of a Gaussian kernel was chosen to fit the ESC of the projection of a lead block on top of a lucite phantom. Estimated scatter fields are obtained by convolving the original projection images with the Gaussian kernel. Two potential drawbacks can be addressed to this method in general: a uniform scatter kernel may not yield a successful estimation of scatter at every region in the projection images, and the convolution is applied to the primary-plus-scatter image not the primary-only image. However, in small animal imaging, the object size is sufficiently small to neglect the regional differences of scatter convolution and the scatter fraction is small enough to keep the errors tolerable in scatter estimation possibly induced by convolving the primary-plus-scatter images.

Various approaches for inversion of Eq. (6) have been proposed in the past. They include an approximation of the transmission by nonlinear equations[25], a direct approximation of the inverted pathlengths[26], and an isotransmission method[27]. We selected a direct approximation method in this work because it is computationally more efficient, and because it is known to be less sensitive to variation in the transmission data even though its accuracy can be lower than other methods[28]. The calculated images shown in Fig. 8 of thickness maps from the projection images using the proposed dual-energy method appear noisy. We expanded the inversion formula only up to the first order of $(T_{\text{low}} - T_{\text{high}})$ because higher order terms of $(T_{\text{low}} - T_{\text{high}})$ would increase the noise even more in the inverted results. Physical origin of this high sensitivity of the inversion equations to input variables is thought to come from insufficient separation of the X-ray energy spectra used in this work[29]. Although the noise reduction problem remains for the future work, the results presented here are believed to show the feasibility of dual-energy imaging for low kV X-ray radiographic systems.

Due to power limitation of the X-ray tubes used for specimen imaging, it takes in general much longer to achieve enough exposure per single projection than a commercial micro-CT system.

NIH-PA Author Manuscript

NIH-PA Author Manuscript

NIH-PA Author Manuscript

This hinders a fast volumetric, dual energy CT imaging in a prototype CT system based on a specimen radiographic system. A 3-D image reconstruction method from a few view projections such as a total-variation minimization algorithm[30] may be found to be very useful in this application.

References

[1]. Grodzins L. Optimum energies for X-ray transmission tomography. Nucl. Inst. Meth 1983;206:541–545.

[2]. Chen AS, Marsh DJ, Trumbauer ME. Inactivation of the mouse melanocortin-3 receptor results in increased fat mass and reduced lean body mass. Nature Genet 2000;26:97–102. [PubMed: 10973258]

[3]. Giakos GC, Chowdhury S, Shah N, et al. Signal evaluation of a novel dual-energy multimedia imaging sensor. IEEE Trans. Instrum. Meas 2002;51:949–954.

[4]. Hassler U, Garnero L, Rizo P. X-ray dual-energy calibration based on estimated spectral properties of the experimental system. IEEE Trans. Nucl. Sci 1998;45:1699–1712.

[5]. Heismann BJ, Leppert J, Stierstorfer K. Density and atomic number measurements with spectral X-ray attenuation method. J. Appl. Phys 2003;94:2073–2079.

[6]. Jiang, H. Computed Tomography-Principles, Designs, Artifacts, and Recent Advances. SPIE Press; Bellingham, WA: 2003.

[7]. Engler P, Friedman WD. Review of dual-energy computed tomography techniques. Mater. Eval 1990;48:623–629.

[8]. Baird LC. X-ray spectra vs attenuation data: A theoretical analysis. Med. Phys 1981;8:319–323. [PubMed: 7322056]

[9]. Huang PH, Chen TS, Kase KR. Reconstruction of diagnostic X-ray spectra by numerical analysis of transmission data. Med. Phys 1986;13:707–710. [PubMed: 3785000]

[10]. Boone JM. X-ray spectral reconstruction from attenuation data using neural networks. Med. Phys 1990;17:647–654. [PubMed: 2215410]

[11]. Ruth C, Joseph PM. Estimation of a photon energy spectrum for a computed tomography scanner. Med. Phys 1997;24:695–702. [PubMed: 9167160]

[12]. Waggener RG, Blough MM, Terry JA, et al. X-ray spectra estimation using attenuation measurements from 25 kVp to 18 MV. Med. Phys 1999;26:1269–1278. [PubMed: 10435529]

[13]. Yan CH, Whalen RT, Beaupré GS, et al. Modeling of polychromatic attenuation using computed tomography reconstructed images. Med. Phys 1999;26:631–642. [PubMed: 10227366]

[14]. Sidky EY, Yu LF, Pan XC, et al. A robust method of x-ray source spectrum estimation from transmission measurements: demonstrated on computer simulated, scatter-free transmission data. J. Appl. Phys 2005;97(12):124701-1–124701-11.

[15]. Coljin AP, Zbijewski W, Sasov A, et al. Experimental validation of a rapid Monte Carlo based micro-CT simulator. Phys. Med. Biol 2004;49:4321–4333. [PubMed: 15509068]

[16]. Attix, FH. Introduction to Radiological Physics and Radiation Dosimetry. Wiley-VCH; Germany: 1986.

[17]. Hubbell, JH.; Seltzer, SM. Technical Report 5632, NIST. Ionizing Radiation Division, Physics Laboratory National Institute of Standards and Technology; Gaithersburg, MD, USA: 1996. Tables of X-ray Mass Attenuation Coefficients and Mass Energy-absorption Coefficients 1 keV to 20 MeV for Elements Z = 1 to 92 and 48 Additional Substances of Dosimetric Interest.

[18]. Black, N.; Gregor, J. Monte Carlo simulation of scatter in a cone-beam micro-ct scanner. Proceedings of the 8th International Conference on Fully Three-Dimensional Image Reconstruction in Radiology and Nuclear Medicine; Salt Lake, USA. 2005. p. 207-210.

[19]. Love LA, Kruger RA. Scatter estimation for a digital radiographic system using convolution filtering. Med. Phys 1987;14:178–185. [PubMed: 3587135]

[20]. Kruger DG, Zink F, Peppler WW, et al. A regional convolution kernel algorithm for scatter correction in dual-energy images: Comparison to single-kernel algorithms. Med. Phys 1994;21:175–184. [PubMed: 8177150]

NIH-PA Author Manuscript

NIH-PA Author Manuscript

NIH-PA Author Manuscript

[21]. Seibert JA, Boone JM. X-ray scatter removal by decon-volution. Med. Phys 1988;15:567–575. [PubMed: 3211049]

[22]. Zbijewski W, Beekman FJ. Efficient Monte Carlo based scatter artifact reduction in cone-beammicro-CT. IEEE Trans. Med. Imag 2006;25:817–827.

[23]. Kyriakou Y, Riedel T, Kalender WA. Combining deterministic and Monte Carlo calculations for fast estimation of scatter intensities in CT. Phys. Med. Biol 2006;51:4567–4586. [PubMed: 16953043]

[24]. Zhu L, Bennett NR, Fahrig R. Scatter correction method for X-ray CT using primary modulation: Theory and preliminary results. IEEE Trans. Med. Imag 2006;25:1573–1587.

[25]. Alvarez RE, Macovski A. Energy-selective reconstructions in X-ray computerized tomography. Phys. Med. Biol 1976;21:733–744. [PubMed: 967922]

[26]. Brody WR, Butt G, Hall A, et al. A method for selective tissue and bone visualization using dual energy scanned projection radiography. Med. Phys 1981;8:353–357. [PubMed: 7033756]

[27]. Chuang KS, Huang HK. A fast dual-energy computational method using isotransmission lines and table lookup. Med. Phys 1987;14:186–192. [PubMed: 3587136]

[28]. Chuang KS, Huang HK. Comparison of four dual energy image decomposition methods. Phys. Med. Biol 1988;33:455–466.

[29]. Kelcz F, Joseph PM, Hilal SK. Noise considerations in dual energy CT scanning. Med. Phys 1979;6:418–425. [PubMed: 492076]

[30]. Sidky EY, Kao CM, Pan X. Accurate image reconstruction from few-views and limited-angle data in divergent-beam CT. J. X-ray Sci. Technol 2006;14:119–139.

NIH-PA Author Manuscript

NIH-PA Author Manuscript

NIH-PA Author Manuscript

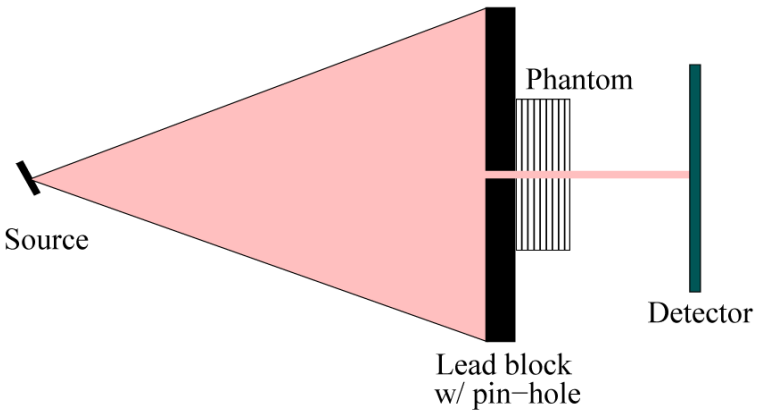

Fig. 1.
Narrow beam geometry used in transmission measurements

NIH-PA Author Manuscript

NIH-PA Author Manuscript

NIH-PA Author Manuscript

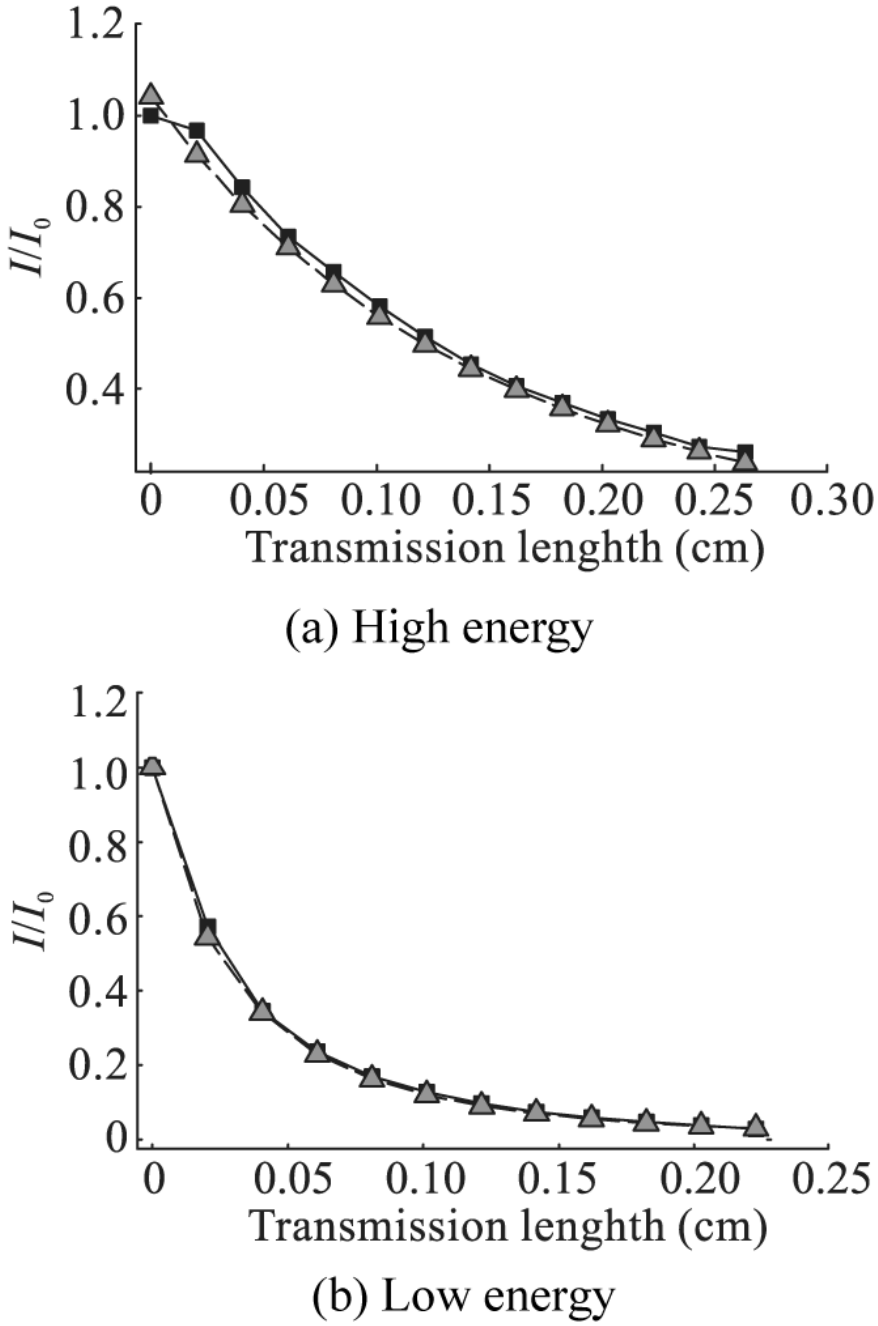

Fig. 2.

Transmission data for aluminum with high energy spectrum of X-ray source and with low energy spectrum. Measured data are represented by solid squares, and calculated data from the estimated spectra are represented by solid triangles.

NIH-PA Author Manuscript

NIH-PA Author Manuscript

NIH-PA Author Manuscript

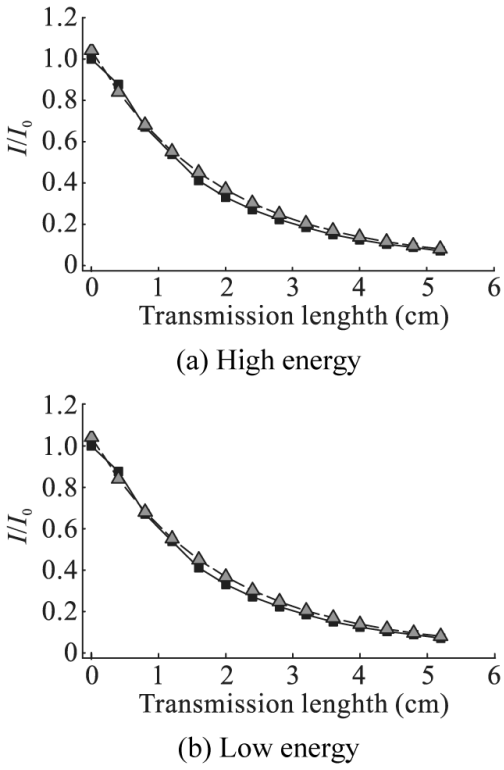

Fig. 3.

Transmission data for lucite with high energy spectrum of X-ray source and with low energy spectrum. Measured data are represented by solid squares, and calculated data from the estimated spectra are represented by solid triangles.

NIH-PA Author Manuscript

NIH-PA Author Manuscript

NIH-PA Author Manuscript

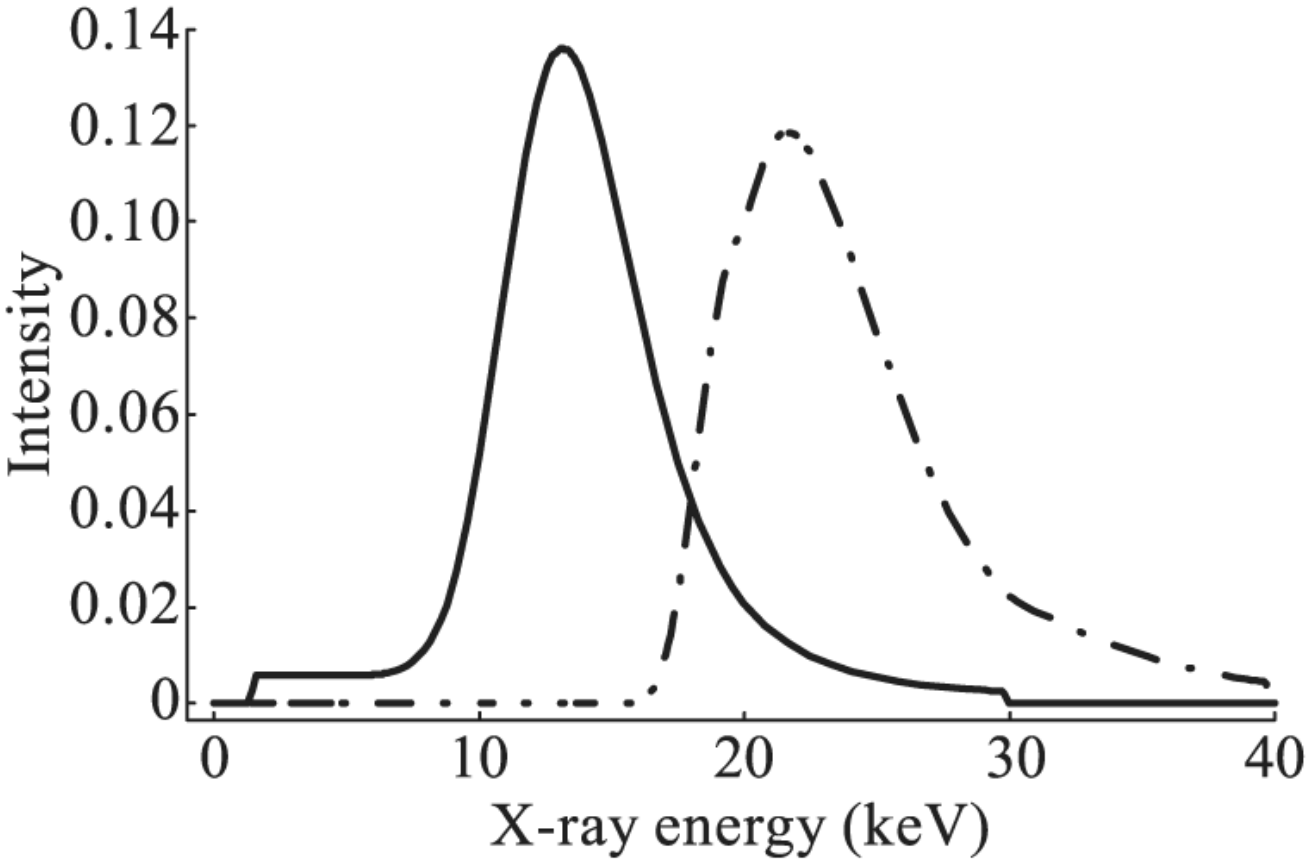

Fig. 4.
Estimated spectra of the X-ray beam. Solid line represents the low energy spectrum at the tube voltage of 22 kV, and dash-dot line represents the high energy spectrum at the tube voltage of 35 kV.

NIH-PA Author Manuscript

NIH-PA Author Manuscript

NIH-PA Author Manuscript

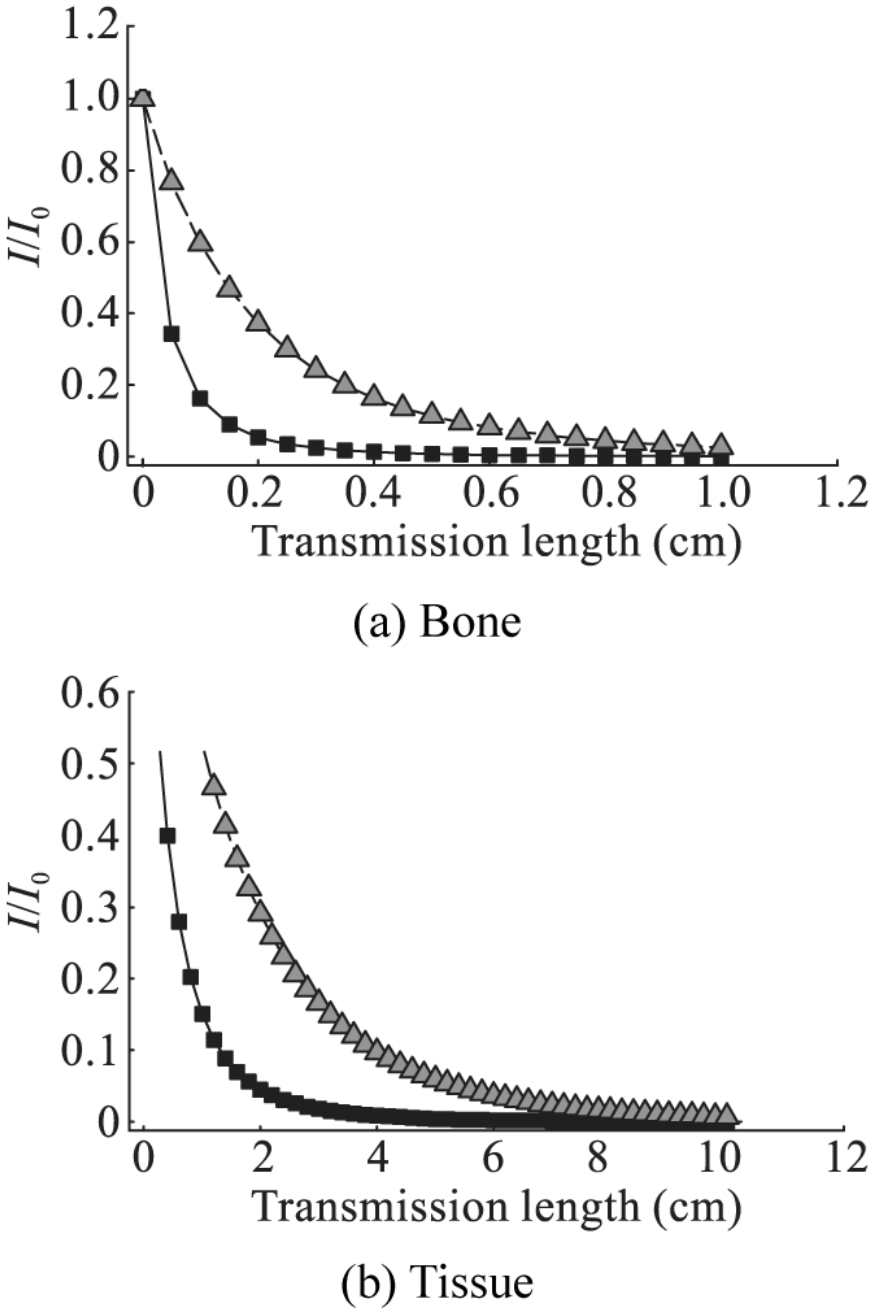

Fig. 5.
Calculated transmission data for bone and for tissue. Solid square represents the data for high energy spectrum of X-ray source, and solid triangle represents the data for low energy spectrum.

NIH-PA Author Manuscript

NIH-PA Author Manuscript

NIH-PA Author Manuscript

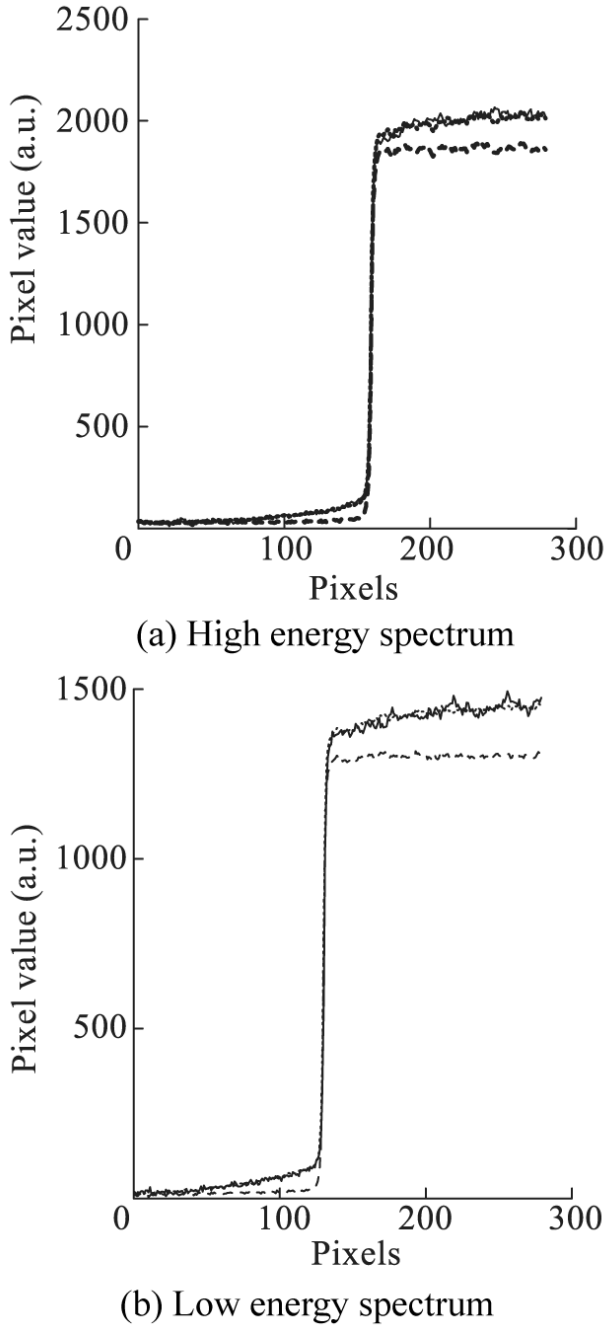

Fig. 6.

Measured primary beamprofiles (dashed), measured primary-plus-scatter beam profiles (solid), and the fitted results (dotted) using a Gaussian convolution at high energy spectrum and low energy spectrum, respectively

NIH-PA Author Manuscript

NIH-PA Author Manuscript

NIH-PA Author Manuscript

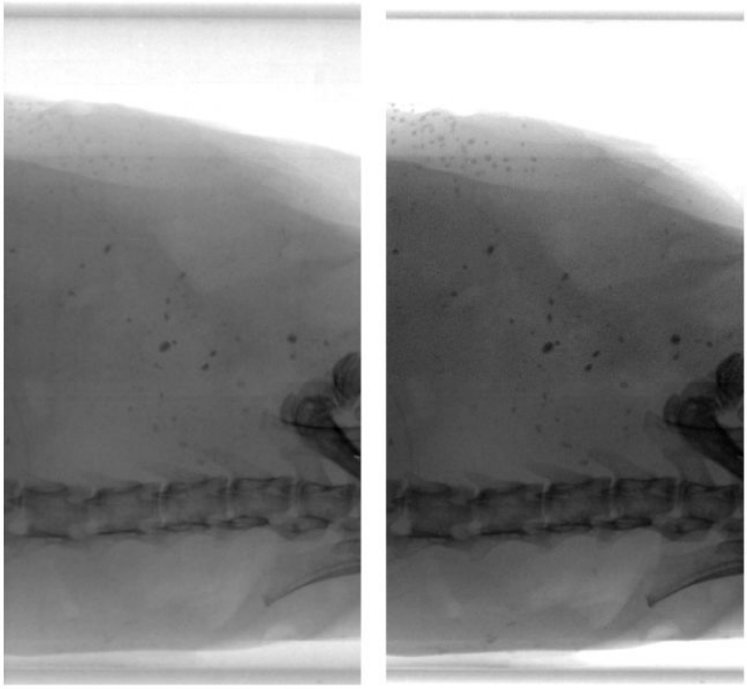

Fig. 7.
Projection image of the mouse at high energy spectrum (left) and at low energy spectrum (right)

NIH-PA Author Manuscript

NIH-PA Author Manuscript

NIH-PA Author Manuscript

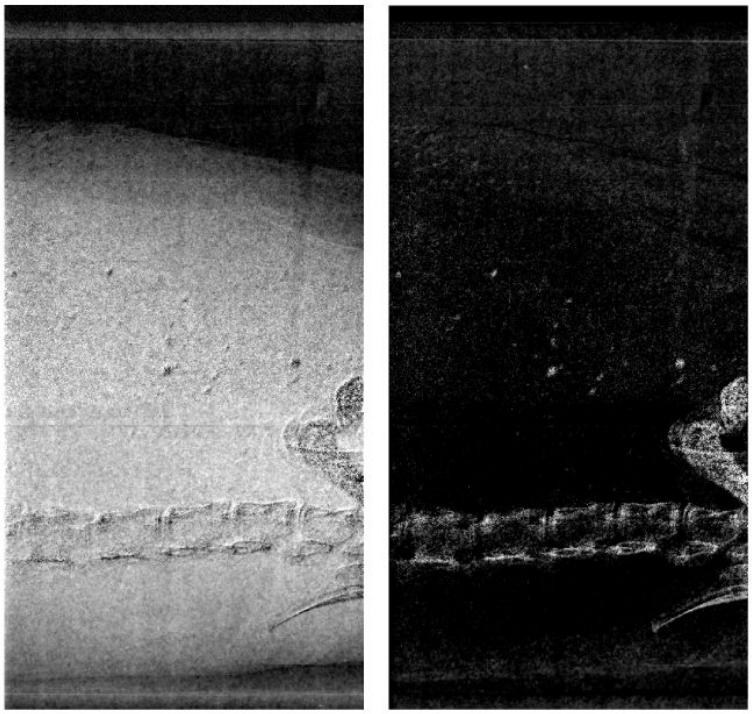

Fig. 8.
Tissue thickness map (left) and bone thickness map (right) calculated from the transmission data

NIH-PA Author Manuscript
NIH-PA Author Manuscript
NIH-PA Author Manuscript

Table 1

The parameters in Eq. (7) used for the dual-energy method in this paper

i	a_{ij}		i	b_{ij}	
	j=0	j=1		j=0	j=1
0	-1.566×10^{-3}	2.497×10^{-1}	0	1.218×10^{-2}	−2.038
1	-7.522×10^{-1}	3.234×10^{-1}	1	7.653	−2.685
2	-2.734×10^{-1}	1.201×10^{-1}	2	2.493	-8.345×10^{-1}
3	-2.696×10^{-1}	5.191×10^{-2}	3	1.555	-2.950×10^{-1}
4	1.138×10^{-1}	-3.100×10^{-2}	4	-7.676×10^{-1}	2.116×10^{-1}
5	-1.059×10^{-2}	3.195×10^{-3}	5	7.417×10^{-2}	-2.267×10^{-2}